GNSS/Onboard Inertial Sensor Integration With the Aid of 3-D Building Map for Lane-Level Vehicle Self-Localization in Urban Canyon

Yanlei Gu, *Member, IEEE*, Li-Ta Hsu, *Member, IEEE*, and Shunsuke Kamijo, *Member, IEEE*

***Abstract*—Lane-level vehicle self-localization is a challenging and significant issue arising in autonomous driving and driver-assistance systems. The Global Navigation Satellite System (GNSS) and onboard inertial sensor integration are among the solutions for vehicle self-localization. However, as the main source in the integration, GNSS positioning performance is severely degraded in urban canyons because of the effects of multipath and non-line-of-sight (NLOS) propagations. These GNSS positioning errors also decrease the performance of the integration. To reduce the negative effects caused by GNSS positioning error, this paper proposes to employ an innovative GNSS positioning technique with the aid of a 3-D building map in the integration. The GNSS positioning result is used as an observation, and this is integrated with the information from the onboard inertial sensor and vehicle speedometer in a Kalman filter framework. To achieve stable performance, this paper proposes to evaluate and consider the accuracy of the employed GNSS positioning method in dynamic integration. A series of experiments in different scenarios is conducted in an urban canyon, which can demonstrate the effectiveness of the proposed method using various evaluation and comparison processes.**

***Index Terms*—Global Navigation Satellite System (GNSS) positioning accuracy, Kalman filter, sensor integration, vehicle self-localization.**

I. Introduction

VEHICLE self-localization is an important and challenging issue in current driving assistance and autonomous driving research activities. Beyond the correct road segment identification, lane-level localization enables more precise guiding along the desired trajectory. In addition, if there is more than one vehicle on the road, the accurate knowledge of vehicle position will ensure the safe operation of vehicle cooperation. Thus, a vast number of localization proposals can be found in the literature, which employed sophisticated methods to achieve high accuracy.

A straightforward and commonly followed approach of the localization problem is to use the integration of a Global Navigation Satellite System (GNSS) and an inertial navigation system (INS). The Global Positioning System (GPS, i.e., one kind of GNSS) should be the main navigation information source for autonomous vehicles, due to its capability of positioning a circulating vehicle in real time with enough accuracy and without temporal precision degradation, which was indicated from the famous DARPA Grand Challenge [1]. In the open-sky field, i.e., eight satellites or more, the error standard deviation of differential-mode GPS positioning is about 30 cm [2]. However, the land vehicle navigation system typically has to operate in the areas where GNSS signals are either blocked or reflected.

An INS is a navigation aid that uses multiple onboard sensors, such as accelerometers and gyrosensors, to continuously calculate via dead reckoning the position, orientation, and velocity of a moving object. In addition, the vehicle speedometer can be used as an external aid for the INS. The INS can provide accurately relative vehicle position in a short time, but its accuracy degrades with time. To overcome the disadvantages associated with the standalone operation of GNSS and INS, the two systems are often integrated together, so that their drawbacks are minimized. In the early studies of this integration field, the research studies focused on evaluating the integration system performance under open-sky fields [3]–[5]. Recently, the qualification of the integration system has been discussed and performed in a more difficult environment. To overcome the multipath interference when the GPS signal is blocked by external agents, Milanes *et al.* proposed a dynamic integration system using a decision unit, which can choose the correct one from GPS and INS [6]. Godha *et al.* employed constraints to describe the behavior of a typical land vehicle in the GPS/INS integrated system, when a GPS outage occurred in urban areas [7]. Noureldin *et al.* improved the microelectromechanical system (MEMS)-based inertial sensor errors to enhance the positioning accuracy during GPS outage [8]. Kubo and Dihan used the information of inertial sensors to aid Real-Time Kinematic (RTK) to estimate the ambiguity solution in an urban area [9].

In fact, the two effects, i.e., non-line-of-sight (NLOS) and multipath, often happen together in urban canyons, but they are not the same. Fig. 1 illustrates both phenomena. In the case of NLOS, the signal is only received via reflection, no direct line-of-sight (LOS) path exists. The multipath means that the direct path and reflected path are received together. Various technologies of GNSS were developed to mitigate the multipath effects, which are mainly cataloged by three: antenna-based

Manuscript received December 22, 2014; accepted October 26, 2015. Date of publication November 2, 2015; date of current version June 16, 2016. The review of this paper was coordinated by Dr. Y. Gao.

The authors are with The University of Tokyo, Tokyo 153-8505, Japan (e-mail: guyanlei@kmj.iis.u-tokyo.ac.jp; qmohsu@kmj.iis.u-tokyo.ac.jp; kamijo@iis.u-tokyo.ac.jp).

Color versions of one or more of the figures in this paper are available online at http://ieeexplore.ieee.org.

Digital Object Identifier 10.1109/TVT.2015.2497001

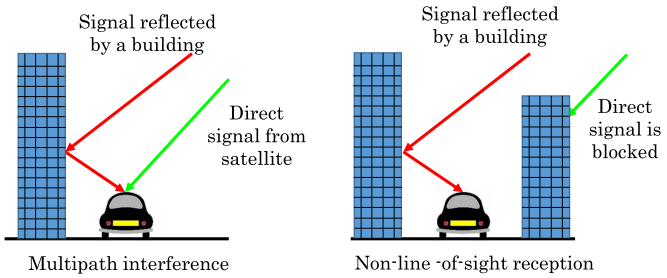

Fig. 1. Multipath interference and NLOS reception, inspired by [17].

[10], [11]; receiver-based [12], [13]; and navigation-processor-based [14]–[16] techniques. The ranging measurement errors that result from NLOS reception are quite different from those produced by multipath interference, and these are not corrected by most multipath mitigation techniques [17].

With the development of ranging technologies, the 3-D building information became available to estimate the multipath and NLOS effects. Meguro *et al.* used an omnidirectional infrared (IR) camera, which was installed on the roof of vehicles, for estimating the area of sky and identifying NLOS signals [18]. As an extended idea of NLOS exclusion, Bauer *et al.* built a shadow map, which can represent the satellite reception conditions in real time [19]. The NLOS measurement can be detected and excluded from the positioning solution [19]. Moreover, Obst *et al.* utilized a dynamic 3-D map to exclude the potential multipath signal from the observation set for a vehicle-based loosely coupled GNSS/INS integration system [20]. In the aforementioned research studies, the positioning accuracy values were improved by excluding the unhealthy signal. However, the skyscrapers locate along the two sides of the road. As a result, the exclusion of satellite will lead to horizontal dilution of precision (HDOP) distortion. Generally speaking, the number of available satellites along the road direction is more than that of the cross direction after exclusion. Thus, the lateral (cross direction) positioning error would be much larger than the longitudinal error (along direction). In the scenario of autonomous driving, distinguishing lanes is significant. In other words, the lateral error should first be considered.

To reduce the effect of the multipath and NLOS while avoiding the distortion of HDOP, our research team developed a candidate-distribution-based positioning method using a 3-D building map for the pedestrian application, which can rectify the positioning result of a commercial GPS single-frequency receiver [21], [22]. After that, the 3-D-building-map-based GPS positioning method was employed for vehicle self-localization application [23]. Moreover, the GLObal NAvigation Satellite System (GLONASS) and Quasi-Zenith Satellite System (QZSS) were introduced to the 3-D-building-map-based method for pedestrian application [24]. In this paper, the 3-D-building-map-based GNSS positioning technique is abbreviated as 3D-Map-GNSS.

One of the most famous urban positioning methods is named shadow matching. The shadow matching method utilizes city building models to predict the satellite visibility and compare this with the measured satellite visibility, to improve the cross-street positioning accuracy [25]–[27]. Recently, RTK GNSS shadow matching based on particle filter is developed [28]. This kinematic GNSS shadow matching describes the likelihood of particles based on the signal strength and satellite visibility. The 3D-Map-GNSS employed in this paper also applies particle filter to estimate receiver position. Moreover, this method takes the advantage of 3-D building map and ray tracing to distinguish the type of signal and further generates the pseudorange correction for the purpose of NLOS and multiple effects. As a result, the likelihood of the particle in this paper is determined by the similarity between corrected pseudorange and pseudorange measurement [22].

This paper proposes to integrate the 3D-Map-GNSS with the onboard inertial sensor and vehicle speedometer to pursue the lane-level accuracy in the vehicle self-localization. Three GNSSs are used, including GPS, GLONASS, and QZSS. In the integration, the positioning result from the 3D-Map-GNSS is considered as observation. The vehicle motion is described by the information derived from a controller area network (CAN) bus of a car and an inertial measure unit (IMU) sensor. This information is integrated by a Kalman filter framework. Moreover, this paper analyzes the principle of the candidate-distribution-based positioning method and develops a way to describe positioning accuracy, user range accuracy $(\mathrm{URA}_{\mathrm{3Dmap}})$, and heading direction accuracy of the 3D-Map-GNSS for the dynamic sensor integration. This proposed sensor integration method is validated by conducting a series of experiments in an urban canyon in Tokyo, Japan.

The remaining part of this paper is organized as follows: Section II analyzes the proposed 3D-Map-GNSS and describes the definition of the accuracy of the 3D-Map-GNSS. Section III presents the integration framework. The experimental results are demonstrated in Section IV. This paper is ended with a conclusion and a future work consideration in Section V.

II. Three-Dimensional-Building-Map-Based Positioning Method

A. Three-Dimensional Building Map and Ray Tracing

To analyze and correct the pseudorange measurement error caused by multipath and NLOS, a 3-D building map is constructed. In this paper, the 3-D building map is shortened to "3-D map." In the establishment of the 3-D map, two sets of map data are required. The first set is the 2-D building outline data named fundamental geospatial data (FGD), which is obtained from the Japan Geospatial Information Authority. The other one is the digital surface model (DSM) data, which is provided by a Japanese company called Aero Asahi Corporation. The DSM data are used for obtaining the height information of the building outline. Fig. 2 illustrates the process of constructing the 3-D map. First, the coordinates of all corners of the building outline are sequentially extracted from FGD, as shown in Fig. 2(a). Then, the height information of each determined corner is derived from DSM data and attached to the corresponding corner. In this way, the 3-D map is generated, which is shown in Fig. 2(b).

Theoretically, the more accurate the 3-D map used, the more accurate pseudorange can be obtained in the ray tracing method. To evaluate the developed 3-D map, an accurate 3-D

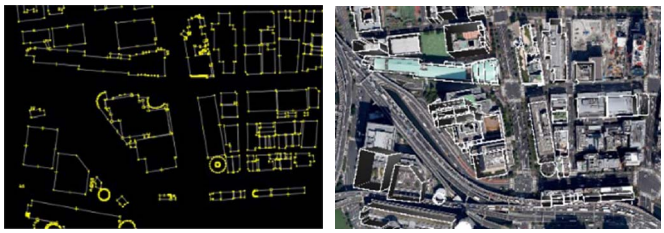

(a) (b)

Fig. 2. Construction of the 3-D building map. (a) Two-dimensional building outline data. (b) Three-dimensional building map.

building model is required as a reference. To obtain a highly accurate 3-D building model, we employed the famous 3-D map mapping company in Japan, which is called Advanced Technology Enables Comfortable Life (A-TEC), to measure the experimental field selected in this paper. The minimum and maximum differences between the reference and developed 3-D building models are about 0.13 and 1 m, respectively. This result shows the resolution of the developed 3-D building model (2-D FGD + 3-D point clouds) is good enough to estimate the reflection path of NLOS signal.

The ray tracing technology was originally designed for the image rendering in computer graphics. Because of the way light propagations resemble those of radio, the ray tracing is also developed and applied in the research of radio propagation [29]. In this paper, the 3D-Map-GNSS method assumes that a building surface is a mirrorlike smooth surface, which can completely reflect the signal. Suppose that satellite position, receiver position, and building surface position are known, the intersection between building surface and reflection path can be estimated. If the intersection exists in the range of a building surface, then the signal reflection is identified. This developed ray tracing simulation can be used to distinguish reflected rays and to estimate the reflection delay distance. In addition, this paper only considers single reflection because the more reflection that the signal traveled, the higher noise will be contained in the ray tracing method.

B. Positioning Rectification Using Candidate Distribution

The ray tracing method provides a solution to estimate the reflection delay distance. Theoretically, the simulated pseudorange from the receiver position and the pseudorange measurement should be the same. Based on this assumption, the 3D-Map-GNSS positioning technique adopts a candidate distribution method for the positioning rectification. First, this positioning method distributes a number of positioning candidates. Then, the validity and likelihood of each candidate are evaluated. Finally, the rectified position is determined by considering the likelihood of all the valid candidates. The flowchart of this method is demonstrated in Fig. 3. This paper will briefly explain the rectification process, and the more detailed description can be found in our previous works [21], [22].

The first step of this positioning method is to generate positioning candidates. In the research, the commercial GNSS receiver is employed for providing "raw" user position and pseudorange measurement. This raw user positioning is considered as one center of the distribution of candidates. Moreover, to reduce the effect of the error of "raw" user position, the predicted position is adopted as the other center of candidate distribution. The prediction can be estimated from the onboard inertial sensors in the vehicle application.

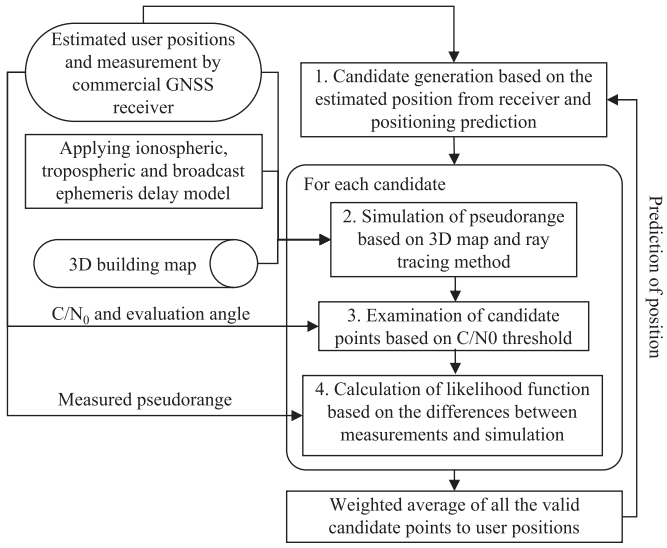

Fig. 3. Flowchart of the 3-D-building-map-based rectification positioning method.

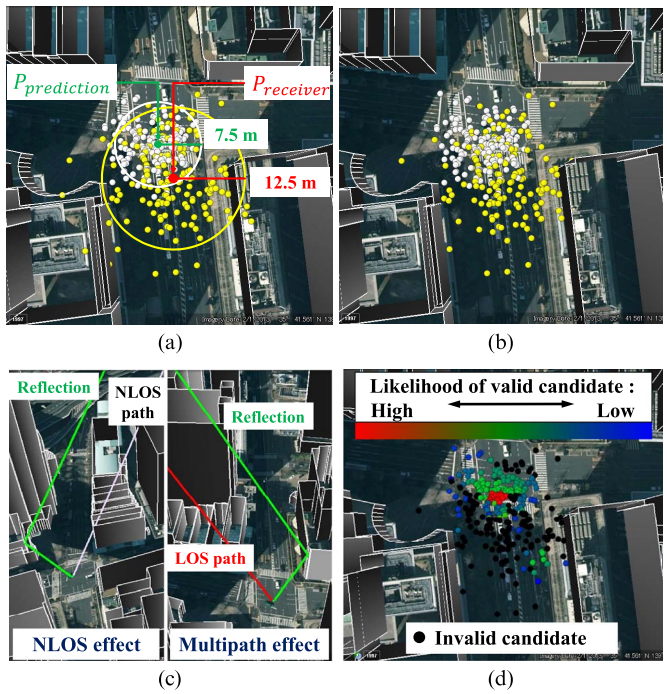

Fig. 4. Candidate distribution and likelihood evaluation. (a) Distribution of candidates. (b) Exclusion of candidates. (c) NLOS and multipath effects visualized by ray tracing. (d) Valid and invalid candidates.

Then, the Gaussian random candidates are generated with one half based on the "raw" user position provided by the GNSS receiver and the other half based on the predicted user position. The principle of the candidate distribution is illustrated in Fig. 4(a). The distribution radius of the first half of candidates is

set as 12.5 m, based on the performance of the positioning result of the employed commercial receiver. The spread radius of the remaining half of candidates is 7.5 m, to allow the prediction error. In this paper, the number of candidates is 300. This value is empirically chosen to balance computation load and positioning performance.

Second, after the candidate points are generated, the ray tracing is employed to calculate the simulated pseudorange from each candidate point, to evaluate the similarity with the original pseudorange measurement provided by the receiver. The calculation of the simulated pseudorange is shown as the following equation:

$$\hat{\rho}_n^{(i)} = R_n^{(i)} + c\left(\delta t^{\mathrm{r}(i)} - \delta t_n^{\mathrm{sv}}\right) + I_n + T_n + \varepsilon_n^{\mathrm{refl}(i)} \tag{1}$$

where $R_n^{(i)}$ denotes the geometric distance between the satellite n and the simulated sample i, $c\delta t^{\mathrm{r}(i)}$ is the receiver clock offset equivalent distance, and $c\delta t_n^{\mathrm{sv}}$ is the satellite clock offset equivalent distance. I_n is the ionospheric delay, T_n is the tropospheric delay, and $\varepsilon_n^{\mathrm{refl}(i)}$ denotes the reflection delay distance estimated by the ray tracing method. In this paper, the satellite clock offset δt_n^{sv} is corrected using the QZSS L1-SAIF fast and long-term corrections [30]. The ionospheric delay I_n is obtained from the ionospheric grid point (IGP) delay model provided by the QZSS L1-SAIF signal [30]. The tropospheric delay T_n is calculated based on the Minimum Operational Performance Standards (MOPS) model, which detailed in the Wide Area Augmentation System MOPS [31]. The receiver clock offset δt_n^{sv} is optimized to minimize the difference between the simulated set and the measured set. The reflection delay $\varepsilon_n^{\mathrm{refl}(i)}$ can be divided into three catalogs: LOS, multipath, and NLOS.

Ideally, the LOS signal is not affected by the buildings. Thus, the reflection delay distance $\varepsilon_n^{\mathrm{refl}(i)}$ is zero. In the case of the NLOS, as shown in Fig. 4(c), the calculation of the reflection delay is straightforward, which is the signal reflection path minus the NLOS path. In comparison to the NLOS case, the multipath effect on pseudorange is more ambiguous, which is shown in Fig. 4(c). This paper assumes that the multipath effect is about 6 dB weaker than the LOS signal, and the commercial receiver applies the strobe correlator [32] with 0.2 chip spacing based on the experience. These principles are used to simulate the pseudorange delay caused by multiple paths. In this step, both reflection delay distance and satellite conditions are obtained.

Third, to provide the accurate pseudorange similarity, the condition of each satellite for one candidate is verified based on the signal strength. Generally, the carrier-to-noise density ratio (C/N0) of NLOS signal should be lower than that of LOS signal, and the multiple-path case should be between LOS and NLOS. If the satellite condition determined from the ray tracing is different with the evaluation result based on signal C/N0, then the satellite is excluded from the following similarity calculation process.

Fourth, after satellite condition validation, the satellites that satisfy the aforementioned requirements are selected to calculate the pseudorange similarity. The likelihood of candidate is calculated on the basis of the similarity between the simulated pseudorange and measured pseudorange. This is defined as the following function:

$$\alpha^{(i)}(t) = \begin{cases} \exp\left[-\frac{{D_{\mathrm{Pr}}^{(i)}}^2}{\sigma_0^2}\right], & \left(\text{if } D_{\mathrm{pr}}^{(i)} < C_{\mathrm{pr}}\right) \sim \text{valid} \\ 0, & (\text{otherwise}) \sim \text{invalid} \end{cases} \tag{2}$$

$$D_{\mathrm{Pr}}^{(i)} = \sum_{k=1}^{n} \frac{\left(\mathrm{Pr}_{(k,\mathrm{simulated})}^{(i)} - \mathrm{Pr}_{(k,\mathrm{measured})}\right)}{n} \tag{3}$$

where $a^{(i)}$ denotes the likelihood function of the ith candidate. $D_{\mathrm{Pr}}^{(i)}$ is the averaged difference between the simulated pseudorange and the measured pseudorange. $\mathrm{Pr}_{(k,\mathrm{simulated})}^{(i)}$ denotes the simulated pseudorange for the kth satellite at the ith candidate position, and $\mathrm{Pr}_{(k,\mathrm{measured})}$ is the measured pseudorange of the kth satellite. The averaged difference between the simulated pseudorange of n satellites and the measured pseudorange of n satellites will be used for the calculation of the pseudorange similarity for the candidate i in (2). σ_0 is the variance of $D_{\mathrm{Pr}}^{(i)}$. This paper tunes the variance empirically, and this is set as 20 m^2. To exclude the outlier candidate, this study defines a constant threshold C_{pr}, which is adjusted to 10 m. Fig. 4(d) demonstrates the invalid candidates marked by black color and the valid candidates labeled with different colors to denote different likelihood values.

Finally, the weighted average of the positions of all the valid samples is the final rectified position, as shown in the following equation:

$$\mathbf{x}(t) = \frac{\sum_i \alpha^{(i)}(t)\mathbf{P}^{(i)}(t)}{\sum_i \alpha^{(i)}(t)} \tag{4}$$

where $\mathbf{x}(t)$ denotes the rectified position by the proposed method, and $\mathbf{P}^{(i)}$ denotes the position of the ith candidate. Overall, this method uses the pseudorange similarity of candidate to denote the confidence of the candidate for the final positioning.

C. Accuracy of the 3D-Map-GNSS Method

The 3D-Map-GNSS method provides a solution to correct the positioning error caused by pseudorange delay. To effectively use the positioning result in the integration system, the confidence of the positioning result is expected to be provided. However, the positioning process of the 3D-Map-GNSS is different with the conventional GPS/GNSS positioning method, i.e., weighted least square (WLS). Therefore, it is necessary to discuss the definition of the positioning accuracy for the 3D-Map-GNSS.

In the conventional GPS positioning, the positioning result is calculated using the LOS vector between satellite and receiver to project the pseudorange space to position space. The horizontal positioning accuracy of the conventional GPS positioning is defined as the following equation:

$$\sigma_{\mathrm{GPS}}^2 = \sigma_\rho^2 \times \mathrm{HDOP} \tag{5}$$

where the HDOP is the horizontal dilution of precision, and σ_ρ denotes the user equivalent range error (UERE) [33]. However,

the 3D-Map-GNSS method considers the position and weighting of each valid candidate in positioning, which can also be expressed as

$$\begin{bmatrix} x \\ y \end{bmatrix}_{2\times 1} = \begin{bmatrix} x^{(1)} & y^{(1)} \\ \vdots & \vdots \\ x^{(N)} & y^{(N)} \end{bmatrix}^{T}_{N\times 2} \times \begin{bmatrix} W^{(1)} \\ \vdots \\ W^{(N)} \end{bmatrix}_{N\times 1} \tag{6}$$

where $W^{(i)} = \alpha^{(i)} / \sum_N \alpha^{(N)}$ is the normalized likelihood of a candidate. $[x^{(i)}, y^{(i)}]$ denotes the candidate position. Based on the definition of candidate likelihood in (2), this normalized likelihood represents the pseudorange similarity. Therefore, the 3D-Map-GNSS method projects pseudorange similarity into position space. Referring to definition of the positioning accuracy of conventional GPS and the principle demonstrated in (6), the calculation of the positioning accuracy of the 3D-Map-GNSS method can be expressed as

$$\sigma^2_{3\mathrm{Dmap}} = \left(\overline{D^{(i)}_{\mathrm{pr}}}\right)^2 \times \mathrm{HDOP}_{3\mathrm{Dmap}} \tag{7}$$

where $\overline{D^{(i)}_{\mathrm{pr}}}$ denotes the average of pseudorange similarity of all candidates, which can be considered as the UERE of the 3D-Map-GNSS. Ideally, the smaller pseudorange similarity represents that the estimated position is closer to the ground truth. The $\mathrm{HDOP}_{3\mathrm{Dmap}}$ can be represented by using candidate positions, which is shown as the following equations:

$$H_{3\mathrm{Dmap}} = \begin{bmatrix} x^{(1)} & y^{(1)} \\ \vdots & \vdots \\ x^{(N)} & y^{(N)} \end{bmatrix}_{N\times 2} \tag{8}$$

$$\left(H^T_{3\mathrm{Dmap}} H_{3\mathrm{Dmap}}\right)^{-1} = \begin{bmatrix} \sigma_x^2 & \sigma_{xy} \\ \sigma_{xy} & \sigma_y^2 \end{bmatrix} \tag{9}$$

$$\mathrm{HDOP}_{3\mathrm{Dmap}} = \sqrt{\sigma_x^2 + \sigma_y^2}. \tag{10}$$

To observe (8)–(10), in general, the more number of valid candidates results in the lower value of the $\mathrm{HDOP}_{3\mathrm{Dmap}}$. Based on the aforementioned analysis and definition, the higher accuracy value means that the positioning result has lower confidence.

The number of valid candidates can denote the confidence of the estimated position as well. Ideally, if the center of the candidate distribution is close to the ground truth, the simulated pseudorange of the candidates around the center of distribution will be very similar to the measurement pseudorange. Many valid candidates are supposed to be existing around the area, as shown in Fig. 5(a). Instead, there are few valid candidates that remain after validation, as shown in Fig. 5(b). Based on this analysis, this paper proposes to denote the confidence level

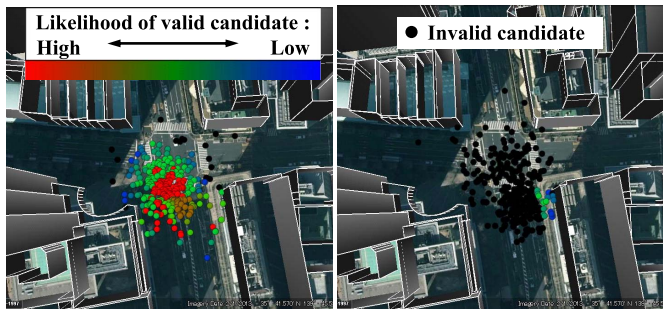

(a) (b)

Fig. 5. Definition of URA ($\mathrm{URA}_{3\mathrm{Dmap}}$) for the 3D-Map-GNSS method. (a) Low-($\mathrm{URA}_{3\mathrm{Dmap}}$) case. (b) High-($\mathrm{URA}_{3\mathrm{Dmap}}$) case.

TABLE I
LEFT: DEFINITION OF URA [34]; RIGHT: $\mathrm{URA}_{3\mathrm{Dmap}}$ USED IN THIS PAPER

URA index	Range Accuracy	$\mathrm{URA}_{3\mathrm{Dmap}}$ index	Percent of the valid candidate
1	2.4 m – 3.4 m	1	75%~100%
2	3.4 m– 4.85 m	2	50%~75%
3	4.85 m – 6.85 m	3	25%~50%
4	6.85 m – 9.65 m	4	10%~25%
5	9.65 m – 13.65 m	5	5%~10%
6	13.65 m – 24.0 m	6	<5%

of the positioning result by the percentage of the valid candidate of all candidates outside the building, as shown in Table I. This idea is similar to the URA of the conventional GPS [34] to indicate its level of positioning service. Thus, the confidence level is named $\mathrm{URA}_{3\mathrm{Dmap}}$ in this paper.

In fact, two sequential GNSS results can indicate the heading direction of the vehicle. Inspired by the developed positioning accuracy, this paper additionally proposes the heading direction accuracy of the 3D-Map-GNSS for a dynamic integration system. Based on the value of $\sigma_{3\mathrm{Dmap}}$ of two sequential GNSS results, the accuracy of the heading direction of the GNSS results, from time $k-1$ to k, can be defined as (11), shown at the bottom of the page.

As shown in Fig. 6, $\mathrm{Dis}^{\mathrm{GNSS}}_{k-1,k}$ is the distance from the GNSS positioning result $\mathbf{GNSS}_{k-1}$ to $\mathbf{GNSS}_k$, which is indicated by the green line. The two blue circles cover the possible positioning area based on the positioning accuracy $(\sigma_{3\mathrm{Dmap},k-1})^2$ and $(\sigma_{3\mathrm{Dmap},k})^2$. The red line, which is the cotangent line of the two circles, has the maximum angle difference relative to the moving direction from $\mathbf{GNSS}_{k-1}$ to $\mathbf{GNSS}_k$. The angle $(\sigma^{\theta}_{3\mathrm{Dmap},k})^2$ is defined as the accuracy of the heading direction of the 3D-Map-GNSS. If there is an overlap between the two blue circles, the $\sigma^{\theta}_{3\mathrm{Dmap},k}$ is equal to π. The main idea of this proposed moving direction accuracy is to indicate the confidence of the moving direction of the 3D-Map-GNSS results.

$$\left(\sigma^{\theta}_{3\mathrm{Dmap},k}\right)^2 = \begin{cases} \left[\arcsin\left(\frac{\sigma_{3\mathrm{Dmap},k}+\sigma_{3\mathrm{Dmap},k-1}}{\mathrm{Dis}^{\mathrm{GNSS}}_{k-1,k}}\right)\right]^2 & \text{if } \sigma_{3\mathrm{Dmap},k}+\sigma_{3\mathrm{Dmap},k-1} < \mathrm{Dis}^{\mathrm{GNSS}}_{k-1,k} \\ \pi^2 & \text{otherwise} \end{cases} \tag{11}$$

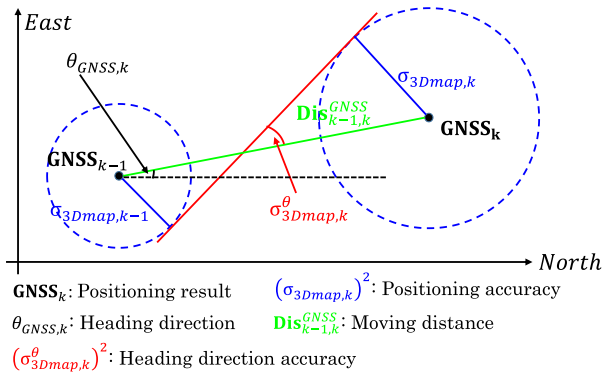

Fig. 6. Accuracy of the heading direction of the 3D-Map-GNSS.

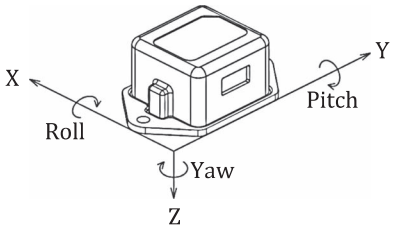

Fig. 7. Definition of angle in the IMU sensor.

III. Sensor Integration

Although the proposed 3D-Map-GNSS can greatly reduce the positioning error, it is difficult to satisfy the lane-level requirement of the vehicle self-localization. The IMU and vehicle speedometer can provide vehicle angle attitude and velocity, respectively. These sensors have an advantage to describe the vehicle motion in a short period of time. Therefore, this paper integrates the IMU sensor and vehicle speedometer (CAN bus data recorder) with the 3D-Map-GNSS method to achieve the lane-level accuracy.

A. IMU Sensor and Integration Coordinate System

This paper employs the north–east–down (NED) coordinate system for the localization calculation. Because the velocity obtained from the CAN bus is the speed in the vehicle body frame. Therefore, the velocity needs to be projected to the NED coordinate system. This research adopts the IMU sensor to detect the angle attitude of the vehicle. This IMU provides not only the acceleration and angle rate but the value of angle along each axis as well. Theoretically, the angle can be calculated using the acceleration and the angle rate information [35]. This paper directly uses the value of the roll and the pitch angle instead of accumulating the angle rate over time.

Based on the specification of the IMU sensor, the roll and pitch angle indicate the angle difference from the IMU body to the horizontal plane that is perpendicular to the direction of gravity, as shown in Fig. 7. The yaw angle is the rotation degree on the Z-axis, which is referred to as the heading direction of the IMU body in this paper. This IMU does not include magnetometers; hence, the value of yaw angle is not the degree relative to the true north in the real-world space. The yaw angle is defined as the accumulated direction changing since

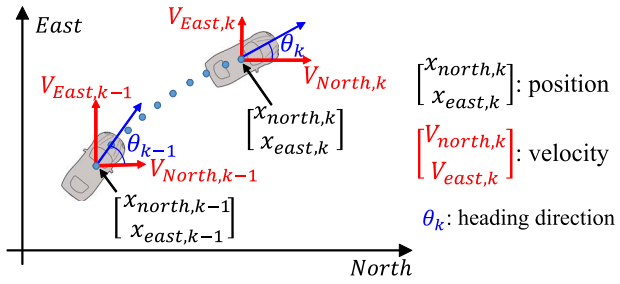

Fig. 8. Vehicle motion on the north–east plane.

the sensor was connected or since the last time this was reset. Suppose that the heading direction has been calibrated relative to the true north direction, the velocity of the vehicle along the north and east directions can be calculated as follows:

$$\begin{bmatrix} V_{\text{north-east}} \\ 0 \\ V_{\text{altitude}} \end{bmatrix} = \begin{bmatrix} \cos(\beta) & 0 & \sin(\beta) \\ 0 & 1 & 0 \\ -\sin(\beta) & 0 & \cos(\beta) \end{bmatrix} \times \begin{bmatrix} 1 & 0 & 0 \\ 0 & \cos(\alpha) & -\sin(\alpha) \\ 0 & \sin(\alpha) & \cos(\alpha) \end{bmatrix} \begin{bmatrix} V_{\text{CAN}} \\ 0 \\ 0 \end{bmatrix} \tag{12}$$

$$\begin{bmatrix} V_{\text{north}} \\ V_{\text{east}} \\ V_{\text{altitude}} \end{bmatrix} = \begin{bmatrix} \cos(\theta) & -\sin(\theta) & 0 \\ \sin(\theta) & \cos(\theta) & 0 \\ 0 & 0 & 1 \end{bmatrix} \begin{bmatrix} V_{\text{north-east}} \\ 0 \\ V_{\text{altitude}} \end{bmatrix} \tag{13}$$

where α is the roll angle, β indicates the pitch angle, θ is the heading direction relative to the direction of true north. The velocity of the vehicle V_{CAN} is decomposed into $V_{\text{north-east}}$ and V_{altitude} in (12). The speed on the north–east plane $V_{\text{north-east}}$ can be further decomposed into V_{north} and V_{east} by the heading direction θ in (13). In fact, it is possible to automatically calibrate the IMU sensor into the north–east plane to obtain the heading direction relative to the north direction [36]. However, directly using the heading angle provided by the IMU sensor generates a drift problem with the increase of time. Therefore, the heading direction is considered as the state in the Kalman filter, and the drift of heading is expected to be mitigated by GNSS positioning results.

B. Integration via Kalman Filter

Because the experiment is conducted in a flat area, the NED coordinate system is simplified as the north–east plane. The original point of the north–east plane is the first epoch of the GNSS positioning result, which is also the start point of the integration. The ego vehicle is described by means of a point position and heading direction in the north–east plane, as shown in Fig. 8. Accordingly, the state vector $\mathbf{X}$ is given by

$$\mathbf{X}_k = \begin{bmatrix} x_{\text{north},k} \\ x_{\text{east},k} \\ \theta_k \end{bmatrix} \tag{14}$$

where $(x_{\text{north},k},\ x_{\text{east},k})$ denote the vehicle position, and θ_k is the heading direction of the vehicle at time k. As shown in

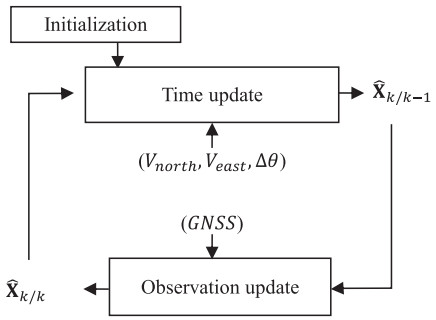

Fig. 9. Kalman filter framework for the integration.

Fig. 8, the movement of the vehicle can be expressed as the following equation:

$$\mathbf{X}_k = \begin{bmatrix} x_{\text{north},k} \\ x_{\text{east},k} \\ \theta_k \end{bmatrix} = \begin{bmatrix} x_{\text{north},k-1} \\ x_{\text{east},k-1} \\ \theta_{k-1} \end{bmatrix} + \begin{bmatrix} \Delta t \cdot V_{\text{north},k-1} \\ \Delta t \cdot V_{\text{east},k-1} \\ \Delta\theta_{k-1} \end{bmatrix} = \begin{bmatrix} x_{\text{north},k-1} \\ x_{\text{east},k-1} \\ \theta_{k-1} \end{bmatrix} + \Delta t \cdot \begin{bmatrix} V_{\text{north-east},k-1} \cdot \cos(\theta_{k-1}) \\ V_{\text{east-east},k-1} \cdot \sin(\theta_{k-1}) \\ \dot{\theta}_{k-1} \end{bmatrix} \tag{15}$$

where $V_{\text{north},k}$ and $V_{\text{east},k}$ denote the velocity along the north and east directions, respectively, at time k. $\Delta\theta_{k-1}$ is the changing of the heading direction from time $k-1$ to k, and $\dot{\theta}_{k-1}$ is the angle rate.

This paper integrates the IMU, vehicle speedometer, and GNSS in a discrete Kalman filter framework. The Kalman filter consecutively locates the vehicle by using the GNSS positioning result and the movement of the vehicle on the north–east plane, as shown in Fig. 9. In general, the velocity and the heading direction changing directly drive the vehicle motion model. This is used to predict the state of the system. The prediction is then combined with the GNSS measurement in the observation update block to produce the estimation of the states. The calculation follows the general Kalman filter algorithm [37].

Based on the vehicle motion model, the system model of the Kalman filter is given by

$$\mathbf{X}_k = F \cdot \mathbf{X}_{k-1} + u_{k-1} + \omega_{k-1} = \begin{bmatrix} x_{\text{north},k} \\ x_{\text{east},k} \\ \theta_k \end{bmatrix} = \begin{bmatrix} 1 & 0 & 0 \\ 0 & 1 & 0 \\ 0 & 0 & 1 \end{bmatrix} \cdot \begin{bmatrix} x_{\text{north},k-1} \\ x_{\text{east},k-1} \\ \theta_{k-1} \end{bmatrix} + \Delta t \begin{bmatrix} V_{\text{north},k-1} \\ V_{\text{east},k-1} \\ \dot{\theta}_{k-1} \end{bmatrix} + \omega_{k-1}. \tag{16}$$

In this model, the control vector u consists of the velocity along the north and east directions and the angle rate. Moreover, the observation of the system is defined as follows:

$$\mathbf{M}_k = H \cdot \mathbf{X}_k + \nu_k = \begin{bmatrix} \text{GNSS}_{\text{north},k} \\ \text{GNSS}_{\text{east},k} \\ \theta_{\text{GNSS},k} \end{bmatrix} = \begin{bmatrix} 1 & 0 & 0 \\ 0 & 1 & 0 \\ 0 & 0 & 1 \end{bmatrix} \cdot \begin{bmatrix} x_{\text{north},k} \\ x_{\text{east},k} \\ \theta_k \end{bmatrix} + \nu_k \tag{17}$$

where $\mathbf{M}_k$ is the GNSS positioning result in the north–east plane, which is used as observation in the Kalman filter. $\theta_{\text{GNSS},k}$ denotes the heading direction of GNSS positioning results from time $k-1$ to k in the north–east coordinate system. In (16) and (17), the random variables ω and ν represent the process and observation noise, respectively. They are assumed to be independent of each other, and they are assumed to be white normal probability distributions, as follows:

$$p(\omega) \sim N(0, Q) \tag{18}$$

$$p(v) \sim N(0, R). \tag{19}$$

The value of element in Q denotes the uncertainty of the system model, and the value of R is the uncertainty of the observed GNSS result. The setting of the value of Q and R can be found in the section of the experiment setup. In the dynamic integration system, the value of R is expressed as follows:

$$\begin{bmatrix} (\sigma_{\text{3Dmap},k})^2 & 0 & 0 \\ 0 & (\sigma_{\text{3Dmap},k})^2 & 0 \\ 0 & 0 & \left(\sigma^{\theta}_{\text{3Dmap},k}\right)^2 \end{bmatrix} \tag{20}$$

where $(\sigma_{\text{3Dmap},k})^2$ and $(\sigma^{\theta}_{\text{3Dmap},k})^2$ correspond to the 3D-Map-GNSS positioning accuracy and heading direction accuracy defined in (7) and (11), respectively.

When the complete outage happens, the GNSS method cannot provide observation for the integration algorithm. In this case, the system will only use the heading direction and the velocity information to propagate. The propagation can be explained by (15). This means that the system completely believes the information obtained from the IMU and speedometer. Recently, many countries have launched their own satellite systems. In addition to the already available GPS and GLONASS constellations and QZSS satellite, Galileo and BeiDou satellites have been available. The multiple GNSSs increase the number of the visible satellites and reduce the probability of outage happening. In this paper, we adopt the multiple-satellite systems (GPS, GLONASS, and QZSS). The multiple-satellite systems have decreased the probability of the outage. Moreover, the integration system monitors the state of the vehicle by the velocity. Here, a simple speed constraint is applied. If the vehicle stops, the integration process will stop. The vehicle position is maintained as the position at the last sampling time.

IV. Experiments

A. Experimental Setup and Error Evaluation

This paper selected the Hitotsubashi area in Tokyo as the experiment spot because of the density of the tall building, as shown in Fig. 10(a). The 3-D map was constructed by the method described in Section II. To demonstrate the effectiveness of the proposed integration method, we repeatedly performed right- and left-turning experiments at different times in a day. Left turning and right turning were performed three times, separately. The driving routes are represented by the cyan line, as shown in Fig. 10(b). The distance of each trajectory is about 700 m.

In the experiment, a high-performance GNSS receiver, i.e., the NovAtel FlexPak-6 GNSS receiver, and a commercial level

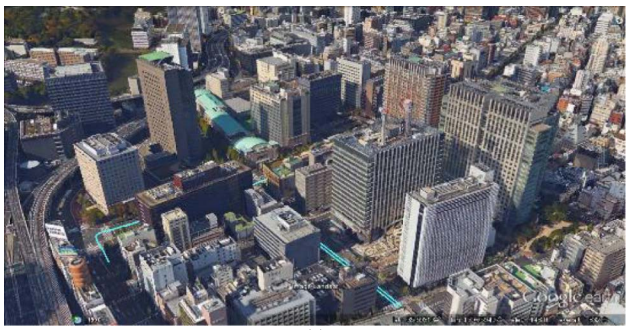

(a)

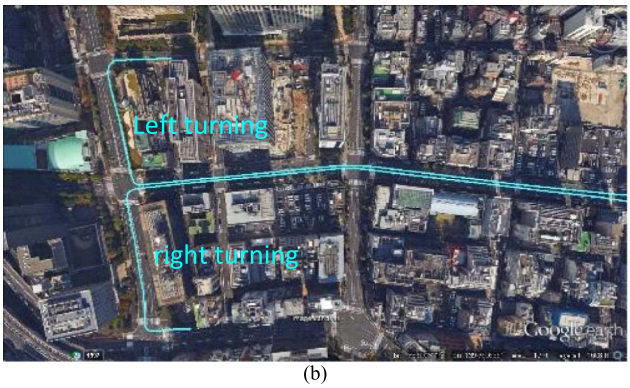

(b)

Fig. 10. Experimental environment and driving routes. (a) Building structure at the experiment spot. (b) Driving routes.

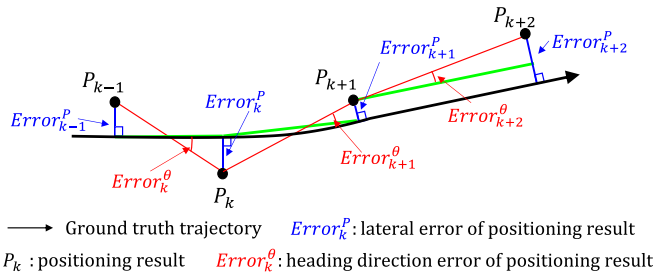

Fig. 11. Demonstration of error evaluation.

receiver, i.e., the u-blox EVK-M8 GNSS model, were used. The NovAtel receiver was only used to collect the QZSS L1-SAIF correction signal. The u-blox receiver was set on the top of the vehicle to provide pseudorange measurements and "raw" positioning results. In addition, the CAN data recorder and IMU sensor (AMU-3002A Lite) were equipped in the experimental vehicle to provide the vehicle velocity and angle information. Moreover, an onboard camera was employed to capture the front-view images of the vehicle. The occupied lane of the experimental vehicle and the ground truth trajectory of the vehicle were distinguished from images captured with the onboard camera. Furthermore, the vehicle was controlled along the center line of occupied lane. In the experiments, the data was collected from the four sensors simultaneously. The computer system time was used for time synchronization. In the vehicle self-localization, it is more important to distinguish which lane the vehicle is. This paper adopts the lateral error to evaluate the performance of the proposed method. As shown in Fig. 11, the lateral error of positioning result P_k is the vertical distance Error_k^P from P_k to the ground truth trajectory.

TABLE II
PERFORMANCE COMPARISON BETWEEN THE WLS AND THE PROPOSED 3D-MAP-GNSS METHOD

	WLS	3D-Map-GNSS	3D-Map-GNSS with $\text{URA}_{\text{3Dmap}} \leq 3$
Mean error (meter)	15.48	2.11	1.98
Standard Deviation (meter)	15.23	1.67	1.54
Maximum error (meter)	78.54	13.41	8.44

In addition, the calculation of the heading direction error Error_k^θ is demonstrated in Fig. 11 as well, which is defined as the angle difference between the heading direction of positioning results and the direction of ground truth trajectory.

B. Evaluation for 3-D Map GNSS Method

This subsection focuses on the evaluation of the performance of the 3D-Map-GNSS positioning method. To understand the benefit of the proposed 3-D building map in an urban canyon environment, this paper compares the positioning results of the WLS and the proposed 3D-Map-GNSS method. The second and third columns in Table II show the quantitative comparison of the WLS and the 3D-Map-GNSS method, which includes the maximum, the mean, and the sample variance of error distance among all left- and right-turning experimental results. This result demonstrates that the proposed 3D-Map-GNSS method reduces the errors dramatically. In particular, the mean error is reduced to about 2.11 m. Moreover, the fourth column in Table II demonstrates that the positioning mean error could be further improved to 1.98 m, by selecting the position points with $\text{URA}_{\text{3Dmap}} \leq 3$.

To understand how much the proposed method can improve the performance compared to WLS, one of the right-turning experimental results is visualized on Google Earth, which is shown in Fig. 12. The Fig. 12(a) shows the positioning result of the WLS. Fig. 12(b) demonstrates the positioning result of the proposed 3D-Map-GNSS method, and the different colors of points represent the $\text{URA}_{\text{3Dmap}}$ level. The cyan line is the ground truth in this experiment. In Fig. 12(a), the positioning results are randomly spread in a wide area, and it is difficult to distinguish the driving route from the experimental result of the WLS. Instead, the positioning result of the 3D-Map-GNSS method is more accurate compared to WLS. In particular, the red points in Fig. 12(b), which have lowest $\text{URA}_{\text{3Dmap}}$ value, are extremely close to the ground truth.

For the explanation of the reason why the proposed method can improve the performance, the condition of satellites used in this experiment is shown in Fig. 12(c). When the GNSS receiver is moving along the right-turning route, it can receive the signals of ten satellites, averagely. About six of the satellites are transmitted as LOS, and the other satellites are as NLOS. If the NLOS signal is used directly, such as WLS, the pseudorange error will be introduced into the positioning process, and positioning error is generated significantly. Due to the proposed GNSS positioning method that uses the 3-D map information, it can distinguish NLOS and rectify the

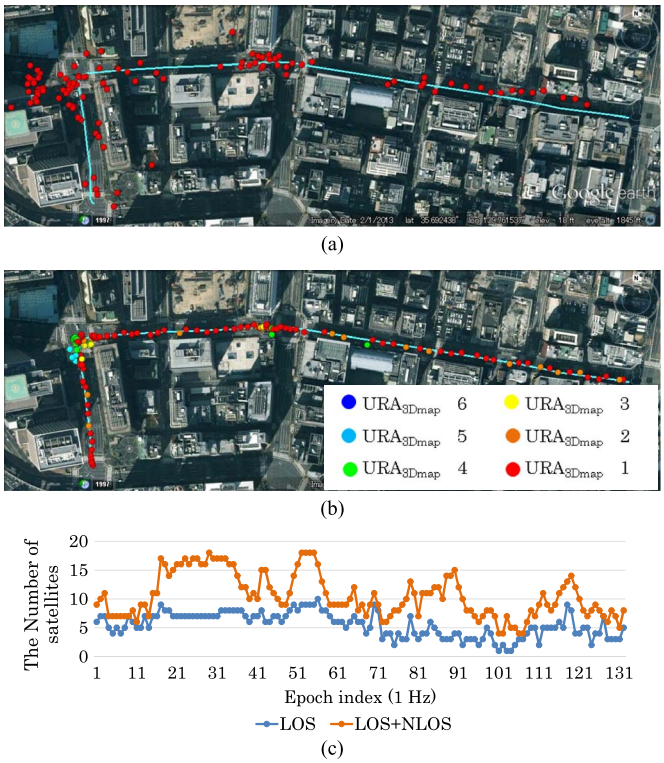

Fig. 12. Visualization of an experimental result in the right-turning case. (a) WLS method. (b) 3D-Map-GNSS method [the different colors on points represent the $\mathrm{URA3_{Dmap}}$ in (b)]. (c) Condition of satellites in the experiment. A blue point indicates the number of satellites transmitted as LOS from the position of ground truth point. An orange point means the number of satellites used in the proposed 3D-Map-GNSS method (LOS + NLOS).

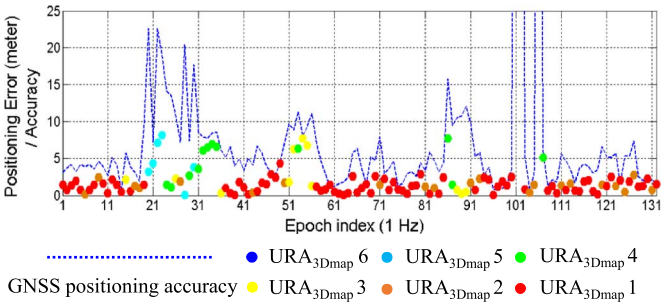

Fig. 13. 3D-Map-GNSS positioning accuracy and positioning error in the experiment illustrated in Fig. 12.

positioning errors. Moreover, the multipath problem is also considered in the proposed method. Therefore, the proposed GNSS positioning method achieves higher performance.

Moreover, Fig. 13 shows the calculated positioning accuracy and positioning error of the 3D-Map-GNSS method, with respect to epoch. The different color points are the corresponding epochs in Fig 12(b). The positioning accuracy is denoted by the blue dash line. Fig. 13 demonstrates that the proposed positioning accuracy and $\mathrm{URA_{3Dmap}}$ can reflect the positioning error. For example, the light blue and green epochs have large positioning error. The positioning accuracy and $\mathrm{URA_{3Dmap}}$ of those epochs are also high. On the contrary, the positioning accuracy, $\mathrm{URA_{3Dmap}}$, and positioning error of red epoch are simultaneously low. This relationship makes the proposed positioning accuracy and $\mathrm{URA_{3Dmap}}$ that can be used in the sensor integration, which can indicate the confidence of the positioning results provided by the 3D-Map-GNSS method.

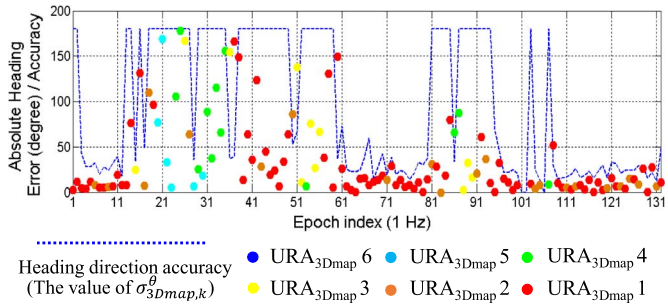

Fig. 14. Heading direction accuracy of the 3D-Map-GNSS and direction error in the experiment illustrated in Fig. 12.

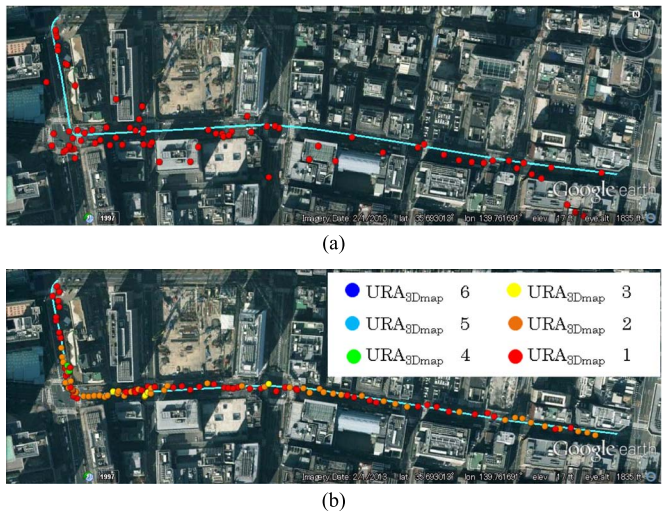

Fig. 15. Visualization of one left-turning experimental result. (a) WLS method and (b) 3D-Map-GNSS method (the different colors on points in (b) denote $\mathrm{URA_{3Dmap}}$).

In addition, Fig. 14 demonstrates the heading direction accuracy of the 3D-Map-GNSS. The blue dash line denotes the value of $\sigma^{\theta}_{3\mathrm{Dmap},k}$ in the heading direction accuracy presented in Section II. The different color points are the corresponding epochs in Fig 12(b) as well, but the meaning of the vertical axis is the direction error. When the direction error is larger, the proposed heading direction accuracy also provides bigger prediction. Throughout all epochs, the changing trend of the heading direction accuracy reflects the degree of the heading direction error of the 3D-Map-GNSS results. This developed heading direction accuracy makes the integration system dynamically decide the observation confidence of the 3D-Map-GNSS heading direction. In addition, Fig. 15 shows another experimental result of the WLS and the 3D-Map-GNSS method in a left-turning scenario. Obviously, the 3D-Map-GNSS has more accurate positioning results.

C. Evaluation for the Performance of Sensor Integration

This subsection focuses on the evaluation of the performance of the sensor integration. The GNSS receiver obtains a sample every 1 s, and the frequency of CAN data and IMU data is

approximately 15 Hz. The integration can increase the sampling frequency. However, to make a direct comparison, this paper evaluates the integration result and the GNSS positioning result at the same sample frequency. The integration starts before entering to the ground truth area. The comparison is conducted among three different integration systems. The first one is the integration of the WLS, IMU, and speedometer. The second one is the integration of the 3D-Map-GNSS, IMU, and speedometer without considering positioning accuracy and $\mathrm{URA}_{3\mathrm{Dmap}}$. The third integration system adopts a dynamic strategy for the 3D-Map-GNSS, IMU, and speedometer integration. In the first and second integration systems, the covariance values of the $\mathrm{GNSS}_{\mathrm{WLS}}$ and $\mathrm{GNSS}_{3\mathrm{Dmap}}$ observation noise are defined as follows:

$$R_{\mathrm{WLS}} = \begin{bmatrix} 15^2 & 0 & 0 \\ 0 & 15^2 & 0 \\ 0 & 0 & \left(\frac{40}{180}\cdot\pi\right)^2 \end{bmatrix}$$

$$R_{3\mathrm{Dmap}} = \begin{bmatrix} 2^2 & 0 & 0 \\ 0 & 2^2 & 0 \\ 0 & 0 & \left(\frac{20}{180}\cdot\pi\right)^2 \end{bmatrix}.$$

The positioning covariance values of the WLS and 3D-Map-GNSS are 15^2 and 2^2 m^2, respectively, which are estimated from Table II. In addition, we evaluated the uncertainty of the heading direction of GNSS positioning results based on multiple data. In the evaluation, the heading direction of two sequential GNSS positioning results is compared with the ground truth to calculate the heading direction error. The standard deviation of the heading direction error of the WLS results is about 40°, and the standard deviation of the heading direction error of the 3D-Map-GNSS result is about 20°. These two values are used in the covariance of observation noise R_{WLS} and $R_{3\mathrm{Dmap}}$. The heading direction accuracy also indicates the advantage of the 3D-Map-GNSS for localization compared to the WLS. The value of the covariance matrix of the system noise Q was tuned for making the system have the best performance. The value of Q is set as follows:

$$Q_{\mathrm{WLS}} = \begin{bmatrix} 1^2 & 0 & 0 \\ 0 & 1^2 & 0 \\ 0 & 0 & \left(\frac{0.1}{180}\cdot\pi\right)^2 \end{bmatrix}$$

$$Q_{3\mathrm{Dmap}} = \begin{bmatrix} 1^2 & 0 & 0 \\ 0 & 1^2 & 0 \\ 0 & 0 & \left(\frac{1}{180}\cdot\pi\right)^2 \end{bmatrix}.$$

This $Q_{3\mathrm{Dmap}}$ is also used for the third integration system. In addition, the third dynamic integration system uses the proposed positioning accuracy, $\mathrm{URA}_{3\mathrm{Dmap}}$, and heading direction accuracy, which have been explained in Section II. Based on the analysis in the last subsection, if the value of the positioning accuracy is larger, the possibility of a large positioning error is higher. In addition, the $\mathrm{URA}_{3\mathrm{Dmap}}$ can also illustrate the confidence level for the positioning result. Thus, the third integration system selects the GNSS positioning results with low $\mathrm{URA}_{3\mathrm{Dmap}}$ value and uses the proposed positioning accuracy and heading direction accuracy for dynamic integration. Table III compares the performance of the three different integration systems and includes the maximum, the mean, and the standard deviation of error as well. The experimental result demonstrates that the integration with 3D-Map-GNSS reduces the error dramatically compared to the WLS-based integration. Moreover, the proposed accuracy and the $\mathrm{URA}_{3\mathrm{Dmap}}$ confidence level can further improve the integration result.

TABLE III
PERFORMANCE COMPARISON OF THE WLS-BASED INTEGRATION AND THE 3D-MAP-GNSS-BASED INTEGRATION

	Integration with WLS	Integration with 3D-Map-GNSS	Integration with 3D-Map-GNSS using accuracy and $\mathrm{URA}_{3\mathrm{Dmap}} \leq 3$
Mean error (meter)	5.83	1.51	1.42
Standard Deviation (meter)	3.91	1.05	0.95
Maximum error (meter)	20.28	5.19	4.94

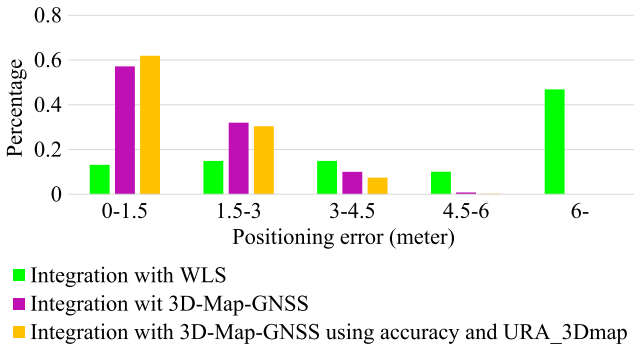

Fig. 16. Positioning error histogram of the WLS-based integration and the proposed 3D-Map-GNSS-based integration.

To deeply understand the improvements, the histogram of positioning error is illustrated in Fig. 16. The horizontal axis of the histogram is the range of positioning error discretized by a half-lane width of 1.5 m. The vertical axis means how much percentage of epochs have the corresponding error. About 50% of the WLS-based integration results have the error more than 6 m. In the integration with 3D-Map-GNSS, about 60% of the positioning results have errors less than the half-lane width. Moreover, the proposed accuracy and $\mathrm{URA}_{3\mathrm{Dmap}}$ reduce the probability of occurrence of large errors in the integration with 3D-Map-GNSS, which can be observed in Fig. 16 as well.

Figs. 17 and 18 visualize the integration results of the three different methods in two experiments that are corresponding to Figs. 12 and 15, respectively. The integration with 3D-Map-GNSS can obtain more accurate positioning results compared to the WLS-based integration, which is easy to be observed. Moreover, Fig. 17(c) presents better positioning results compared to Fig. 17(b), in the white rectangle area, because the dynamic integration strategy was used. This proves that the proposed accuracy and $\mathrm{URA}_{3\mathrm{Dmap}}$ can reduce the effect of the outlier GNSS positioning result in the integration system. This conclusion is in consistency with the result demonstrated in Fig. 16, i.e., the histogram of positioning error.

(a)

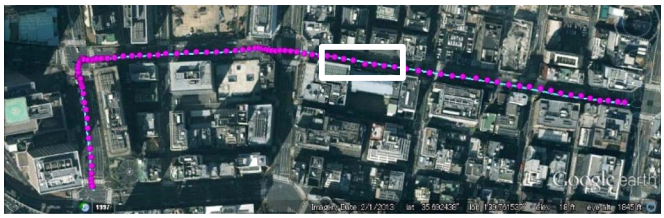

(b)

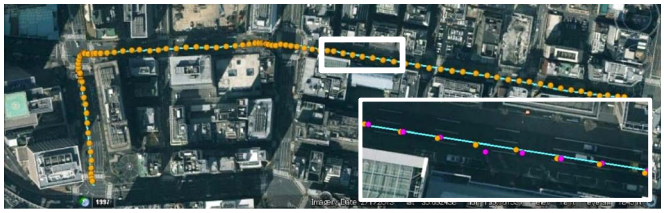

(c)

Fig. 17. Integration results of the different methods in a right-turning case. (a) Integration with WLS. (b) Integration with 3D-Map-GNSS. (c) Integration with 3D-Map-GNSS using positioning accuracy and $\mathrm{URA}_{3\mathrm{Dmap}}$.

(a)

(b)

(c)

Fig. 18. Integration results of the different methods in a left-turning case. (a) Integration with WLS. (b) Integration with 3D-Map-GNSS. (c) Integration with 3D-Map-GNSS using positioning accuracy and $\mathrm{URA}_{3\mathrm{Dmap}}$.

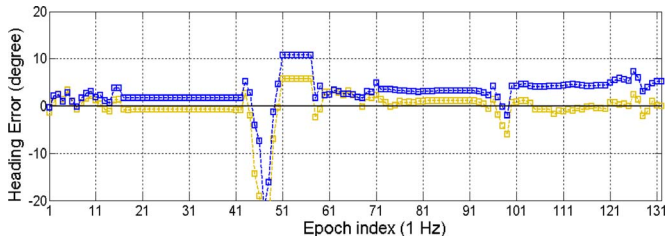

(a)

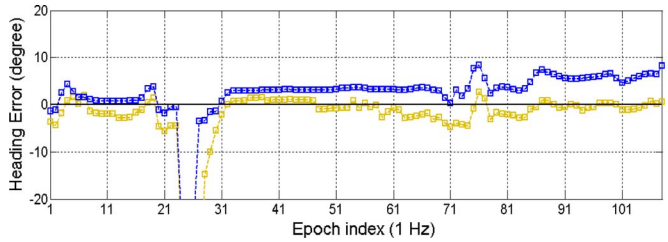

(b)

Fig. 19. Heading direction errors of the IMU and the 3D-Map-GNSS-based integration system. (a) Heading direction errors in the right-turning experiment demonstrated in Fig. 17. (b) Heading direction errors in the left-turning experiment demonstrated in Fig. 18.

With the comparison between Tables II and III, we can conclude that the integration system can improve the positioning result compared to GNSS only. In the integration, GNSS positioning results are used as the observation. The information from the speedometer and IMU sensor smooths the GNSS positioning results, which is observed in Figs. 17 and 18. On the other hand, the observation of GNSS positioning results also mitigates the drift problem of the IMU sensor. Fig. 19 shows the error of the raw heading direction of the IMU sensor and the heading direction error in the 3D-Map-GNSS-based integration system (the state of the Kalman filter), which are indicated by blue and orange lines, respectively. The positive value of error means the angle along the counterclockwise direction. It is clear to see that the heading direction of the IMU sensor has about 5° drift in experiments. However, the heading direction error of the 3D-Map-GNSS integration system changes around zero. This result proves that the integration system also can solve the drift problem. The area between epoch 41 and epoch 61 in Fig. 19(a) and the area between epoch 21 and epoch 31 in Fig. 19(b) are the turning areas. The large error is caused by unconfident ground truth trajectory because it is difficult to manually provide the accurate curve to descript the turning trajectory.

In addition, magnetometers could be another option to provide the absolute heading direction, which can incorporate the IMU to keep the heading drift under control. However, the distribution of the magnetic field in the urban area is complicated. The magnetic deviation is affected not only by the static objects in the surrounding environment, such as buildings and power lines, but by moving objects, such as vehicles, as well. Based on the experiment in our previous work, the magnetic deviation could be 10° [38]. Therefore, it is difficult to provide an accurate heading direction for the integration system by using the magnetometers.

TABLE IV
PERFORMANCE COMPARISON BETWEEN INTEGRATION WITH THE U-BLOX RECEIVER AND INTEGRATION WITH THE 3D-MAP-GNSS

	Integration with u-blox	Integration with 3D-Map-GNSS using accuracy and $URA_{3Dmap} \leq 3$
Mean error (meter)	1.78	1.42
Standard Deviation (meter)	1.50	0.95
Maximum error (meter)	6.54	4.94

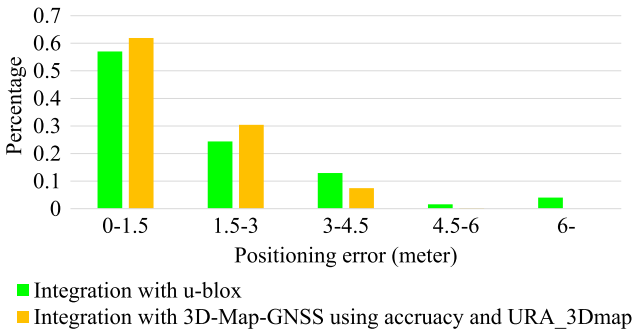

Fig. 20. Positioning error histogram of the u-blox-based integration and the proposed 3D-Map-GNSS-based integration.

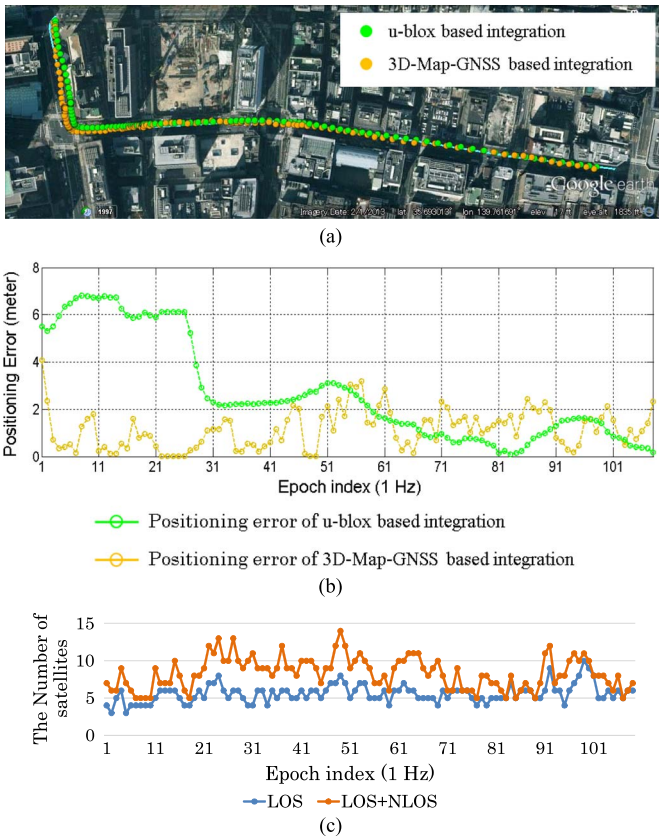

Fig. 21. Visualization of experimental results in the u-blox receiver-based integration and the proposed 3D-map-GNSS-based integration. (a) Integration results of the two integrated systems. (b) Positioning error. (c) Satellite condition in the experiments. A blue point indicates the number of satellites transmitted as LOS from the position of ground truth point. An orange point means the number of satellites used in the proposed 3D-map-GNSS method (LOS + NLOS).

D. Comparison With a Commercial Positioning Device u-Blox

Moreover, this paper makes a comparison between the proposed integration system and one of the famous commercial positioning devices, i.e., the u-blox EVK-M8 GNSS model. The positioning result provided by the u-blox receiver is integrated with the onboard inertial sensor as baseline. Table IV shows the error mean, standard deviation, and maximum error of two integration systems in the experiments. Fig. 20 shows the error histogram of the two integration systems. Both the error mean and the error histogram indicate that the integration with 3D-Map-GNSS achieves the better performance than the u-blox-based integration system. In addition, the dynamic integration with the 3D-Map-GNSS reduces the percentage of occurrence of large error, which is demonstrated in Fig. 20.

To analyze the reason, the integration results of a left-turning case is visualized in Fig. 21, which is corresponding to the experiment demonstrated in Fig. 18. The green points are the u-blox-based integration results. The yellow points denotes the results provided by the proposed integration system. Fig. 21(a) and (b) shows that there is a bias error in the u-blox-based integration before left turning. The condition of satellites used in the experiments is shown in Fig. 21(c). In this experiment, the number of LOS satellites is approximately 4 before turning. This means that the receiver can receive healthy signal from four satellites at most; other received signals may include multipath and NLOS effects. In addition, this left driving route is closer to the building along the left side of the road. Therefore, most satellites at the left side will be blocked. Hence, this pattern of HDOP and pseudorange error is the reason for the bias error in the u-blox integration system. The 3D-Map-GNSS method can rectify the error caused by multipath and NLOS effects, while avoiding the distortion of HDOP. Therefore, the proposed integration system maintains the performance. Although the 3D-Map-GNSS-based integration achieves good performance in an urban canyon, the positioning error of some epochs is larger than 1.5 m. This means that those epochs are located at the neighboring lane. The vision-sensing-based technology could be an option to further improve the positioning result.

V. CONCLUSION AND FUTURE WORK

This paper has proposed to integrate a novel GNSS positioning method with the onboard inertial sensor and vehicle speedometer for the lane-level vehicle localization. The employed GNSS positioning method utilizes the 3-D building map and ray tracing method to rectify pseudorange error caused by NLOS and multipath effects. To use the 3D-Map-GNSS positioning method for the sensor integration, this paper analyzes the employed GNSS method and provides a definition of positioning accuracy, confidence level URA_{3Dmap}, and the heading direction accuracy specifically. In addition, the dynamic integration system is developed. In the integration, the 3D-Map-GNSS provides the observation, and the inertial

sensor and speedometer describe the vehicle motion. This information is dynamically integrated in a Kalman filter framework by considering the accuracy of the 3D-Map-GNSS. A series of experiments and comparisons indicate that the proposed integration system has better performance not only compared to the conventional WLS-based integration but also than the commercial receiver-based integration. The experimental results also demonstrate the proposed system can achieve 1.5-m mean error in the different experiment scenarios.

The experimental results indicate that 60% of the positioning results have half-lane width error (1.5 m). This means that those 60% of positioning results can be used to decide the occupied lane. It is true that the errors of the remaining 40% of positioning results are larger than 1.5 m. The research tried to use the GNSS/INS integration system to achieve the best performance for the vehicle localization in urban environments. We could find the limitation of our sensor configuration at the same time. The experimental results also indicated that most of the positioning results were located at the correct lane or the neighboring lane. This phenomenon inspires us that the vision sensor could be helpful for more accurate results. This will be our future work.

REFERENCES

[1] C. Urmson *et al.*, "A robust approach to high-speed navigation for unrehearsed desert terrain," *J. Field Robot.*, vol. 23, no. 8, pp. 467–508, 2006.

[2] S. Rezaei and R. Sengupta, "Kalman filter-based integration of DGPS and vehicle sensors for localization," *IEEE Trans. Control Syst. Technol.*, vol. 15, no. 6, pp. 1080–1088, Nov. 2007.

[3] F. X. Cao *et al.*, "Low cost SINS/GPS integration for land vehicle navigation," in *Proc. IEEE Conf. Intell. Transp. Syst.*, 2002, pp. 910–913.

[4] A. Kealy, S. Scott-Young, F. Leahy, and P. A. Cross, "Improving the performance of satellite navigation systems for land mobile applications through the integration of MEMS inertial sensors," in *Proc. 14th Int. Tech. Meet. ION GPS*, Salt Lake City, UT, USA, 2001, pp. 1394–1402.

[5] C. D. Hide and T. Moore, "Low cost sensors, High quality integration," in *Proc. NAV/AIS04, Location Timing Appl.*, London, U.K., 2004, pp. 1–10.

[6] V. Milanes, J. E. Naranjo, C. Gonzalez, J. Alonso, and T. de Pedro, "Autonomous vehicle based in cooperative GPS and inertial systems," *Robotica*, vol. 26, no. 5, pp. 627–633, Sep. 2008.

[7] S. Godha and M. E. Cannon, "GPS/MEMS INS integrated system for navigation in urban areas," *GPS Solutions*, vol. 11, no. 3, pp. 193–203, 2007.

[8] A. Noureldin, T. B. Karamat, M. D. Eberts, and A. El-Shafie, "Performance enhancement of MEMS-based INS/GPS integration for low-cost navigation applications," *IEEE Trans. Veh. Technol.*, vol. 58, no. 3, pp. 1077–1096, Mar. 2009.

[9] N. Kubo and C. Dihan, "Availability improvement of RTK-GPS with IMU and vehicle sensors in urban environment," in *Proc. 25th Int. Tech. Meet. ION GNSS*, 2012, pp. 1545–1555.

[10] G. A. Mcgraw, R. S. Y. Young, K. Reichenauer, J. Stevens, and F. Ventrone, "GPS multipath mitigation assessment of digital beam forming antenna technology in a JPALS dual frequency smoothing architecture," in *Proc. Nat. Tech. Meet. Inst. Navig.*, 2004, pp. 561–572.

[11] M. S. Braasch, "Multipath effects," in *Global Positioning System: Theory and Applications*, B. W. Parkinson and J. J. Spilker, Eds. Washington, DC, USA: Amer. Inst. Aeronaut., pp. 547–566, 1996.

[12] A. J. Van Dierendonck, P. Fenton, and T. Ford, "Theory and performance of narrow correlator spacing in a GPS receiver," *Navigation*, vol. 39, no. 3, pp. 265–283, 1992.

[13] M. S. Braasch, "Performance comparison of multipath mitigating receiver architectures," in *Proc. IEEE Conf. Aerosp.*, 2001, vol. 3, pp. 1309–1315.

[14] N. Kubo, T. Suzuki, A. Yasuda, and R. Shibazaki, "An effective method for multipath mitigation under severe multipath environments," in *Proc. 18th Int. Tech. Meet. ION GNSS*, 2005, pp. 2187–2194.

[15] N. Viandier, D. F. Nahimana, J. Marais, and E. Duflos, "GNSS performance enhancement in urban environment based on pseudo-range error model," in *Proc. IEEE/ION Symp. Position, Location Navig.*, 2008, pp. 377–382.

[16] L-T. Hsu, "Integration of vector tracking loop and multipath mitigation technique and its assessment," in *Proc. 26th Int. Tech. Meet. ION GNSS*, 2013, pp. 3263–3278.

[17] P. D. Groves, "GNSS solutions: Multipath vs. NLOS signals. How does non-line-of-sight reception differ from multipath interference?" *Inside GNSS Mag.*, vol. 8, no. 6, pp. 40–42, 2013.

[18] J. I. Meguro, T. Murat, J. I. Takiguchi, Y. Aman, and T. Hashizume, "GPS multipath mitigation for urban area using omnidirectional infrared camera," *IEEE Trans. Intell. Transp. Syst.*, vol. 10, no. 1, pp. 22–30, Mar. 2009.

[19] S. Bauer, M. Obst, R. Streiter, and G. Wanielik, "Evaluation of shadow maps for non-line-of-sight detection in urban GNSS vehicle localization with VANETs—The GAIN approach," in *Proc. IEEE VTC—Spring*, 2013, pp. 1–5.

[20] M. Obst, S. Bauer, P. Reisdorf, and G. Wanielik, "Multipath detection with 3D digital maps for robust multi-constellation GNSS/INS vehicle localization in urban areas," in *Proc. IEEE Symp. IV*, 2012, pp. 184–190.

[21] S. Miura, S. Hisaka, and S. Kamijo, "GPS multipath detection and rectification using 3D maps," in *Proc. IEEE ITSC*, 2013, pp. 1528–1534.

[22] S. Miura, L.-T. Hsu, F. Chen, and S. Kamijo, "GPS Error correction with pseudorange evaluation using three-dimensional maps," *IEEE Trans. Intell. Transp. Syst.*, no. 99, pp. 1–12, Jun. 2015.

[23] Y. Gu, Y. Wada, L.-T. Hsu, and S. Kamijo, "Vehicle self-localization in urban canyon using 3D Map based GPS positioning and vehicle sensors," in *Proc. IEEE ICCVE*, 2014, pp. 792–798.

[24] L.-T. Hsu, Y. Gu, and S. Kamijo, "3D building model based pedestrian positioning method using GPS/GLONASS/QZSS and its reliability calculation," *GPS Solutions*, pp. 1–16, Mar. 2015.

[25] P. D. Groves, "Shadow matching: A new GNSS positioning technique for urban canyons," *J. Navig.*, vol. 64, no. 3, pp. 417–430, 2011.

[26] L. Wang, P. D. Groves, and M. K. Ziebart, "Urban positioning on a smartphone: Real-time shadow matching using GNSS and 3D city models," in *Proc. Inside GNSS Mag.*, 2013, pp. 44–56.

[27] L. Wang, P. D. Groves, and M. K. Ziebart, "GNSS shadow matching: Improving urban positioning accuracy using a 3D city model with optimized visibility scoring scheme," *J. Inst. Navig.*, vol. 60, no. 3, pp. 195–207, Fall 2013.

[28] L. Wang, P. D. Groves, and M. K. Ziebart, "Smartphone shadow matching for better cross-street GNSS positioning in urban environments," *J. Navig.*, vol. 68, no. 3, pp. 411–433, 2014.

[29] H. L. Bertoni, *Radio Propagation for Modern Wireless Systems*. Upper Saddle River, NJ, USA: Pearson, 1999.

[30] T. Saka, S. Fukushima, and K. Ito, "Development of QZSS L1-SAIF augmentation signal," in *Proc. ICCAS-SICE*, 2009, pp. 4462–4467.

[31] "Minimum operational performance standards for global positioning system/wide area augmentation system airborne equipment," Minimum Oper. Perform. Std. (MOPS), Wide Area Augment. Syst. (WAAS), Radio Tech. Commiss. Aeronaut. (RTCA), Washington, DC, USA, RTCA Inc. Doc. No. RTCA/DO-229B, 1999.

[32] L. Garin, F. van Diggelen, and J. M. Rousseau, "Strobe & eEdge correlator multipath mitigation for code," in *Proc. 9th Int. Tech. Meet. ION GPS*, 1996, pp. 657–664.

[33] P. D. Groves, *Principles of GNSS, Inertial, and Multi-Sensor Integrated Navigation Systems (GNSS Technology and Applications)*, 2nd ed. Norwood, MA, USA: Artech House, 2013.

[34] J. J. Spilker, Jr., "GPS navigation data," in *Global Positioning System: Theory and Applications*, B. W. Parkinson and J. J. Spilker, Jr., Eds. Washington, DC, USA: Amer. Inst. Aeronaut., 1996, pp. 121–175.

[35] A. Zul Azfar and D. Hazry, "A simple approach on implementing IMU sensor fusion in PID controller for stabilizing quadrotor flight control," in *Proc. IEEE 7th Int. CSPA*, 2011, pp. 28–32.

[36] Y. Nagasaka, N. Umeda, Y. Kanetai, K. Taniwaki, and Y. Sasaki, "Autonomous guidance for rice transplanting using global positioning and gyroscopes," *Comput. Electron. Agriculture*, vol. 43, no. 3, pp. 223–234, Jun. 2004.

[37] W. Greg and B. Gary, "An introduction to the Kalman filter," Univ. North Carolina, Chapel Hill, NC, USA, Tech. Rep., 2006.

[38] N. Kakiuchi, K. Sunagawa, and S. Kamijo, "Pedestrian dead reckoning for mobile phones using magnetic deviation map," *IEICE Trans. Fundam. Electron., Commun. Comput. Sci.*, vol. E98-A, no. 1, pp. 313–322, 2015.

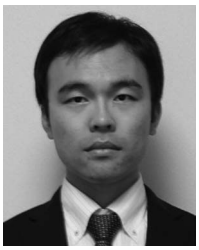

Yanlei Gu (M'14) received the M.E. degree from Harbin University of Science and Technology, Harbin, China, in 2008 and the Ph.D. degree in computer science from Nagoya University, Nagoya, Japan, in 2012.

Since 2013, he has been a Postdoctoral Researcher with the Institute of Industrial Science, The University of Tokyo, Tokyo, Japan. His research interests include computer vision, machine learning, and intelligent transportation systems.

Li-Ta Hsu (S'09–M'15) received the B.S. and Ph.D. degrees in aeronautics and astronautics from the National Cheng Kung University, Tainan, Taiwan, in 2007 and 2013, respectively.

In 2012, he was a Visiting Ph.D. Student with the Faculty of Engineering, University College London, London, U.K. He is currently a Japan Society for the Promotion of Sciences Postdoctoral Fellow with the Institute of Industrial Science, The University of Tokyo, Tokyo, Japan. His research interests include all aspects of Global Navigation Satellite System (GNSS) navigation, positioning, and signal processing, including wide-area differential GNSS systems and improving GNSS performance under challenging reception conditions, and indoor positioning techniques.

Shunsuke Kamijo (M'97) received the B.S. and M.S. degrees in physics and the Ph.D. degree in information engineering from The University of Tokyo, Tokyo, Japan, in 1990, 1992, and 2001, respectively.

In 1992, he was with Fujitsu Ltd., as a Processor Design Engineer. Since 2001, he has been with The University of Tokyo, where he served as an Assistant Professor until 2002 and is currently an Associate Professor. His research interests include computer vision for traffic surveillance by infrastructure cameras and onboard cameras, cooperative systems using vehicle-to-everything (V2X) communication, Global Navigation Satellite System and smartphone applications for intelligent transportation systems (ITS), and marketing.

Dr. Kamijo is a member of the International Program Committee of the ITS World Congress; the Institute of Electronics, Information, and Communication Engineers; the Society of Automotive Engineers of Japan (JSAE); the Japan Society of Civil Engineers; and the International Association of Traffic and Safety Sciences. He is an Editorial Board Member of the *International Journal on ITS Research* (Springer) and *Multimedia Tools and Applications* (Springer).